## **OPEN ACCESS**



# Polarization Analysis of Type III Langmuir/Z-mode Waves with Coherent Magnetic Component Observations by Solar Orbiter

Tomáš Formánek<sup>1,2</sup>, Ondřej Santolík<sup>1,3</sup>, Jan Souček<sup>1</sup>, David Píša<sup>1</sup>, Arnaud Zaslavsky<sup>2</sup>, Matthieu Kretzschmar<sup>4</sup>, Milan Maksimovic<sup>2</sup>, Christopher J. Owen<sup>5</sup>, and Georgios Nicolaou<sup>5</sup>

Czech Academy of Sciences, Institute of Atmospheric Physics, Department of Space Physics, Boční II 1401, Prague 4, Czechia; tomas.formanek@obspm.fr 

<sup>2</sup> LIRA, Observatoire de Paris, Université PSL, CNRS, Sorbonne Université, Université Paris-Cité, Meudon, France 

<sup>3</sup> Charles University, Faculty of Mathematics and Physics, V Holesovickach 2, 18000 Prague 8, Czechia 

<sup>4</sup> LPC2E, OSUC, CNRS/University of Orléans/CNES, 3A avenue de la Recherche Scientifique, 45071 Orléans, France 

<sup>5</sup> Mullard Space Science Laboratory, University College London, Holmbury St Mary, Dorking, Surrey RH5 6NT, UK 

Received 2025 February 21; revised 2025 April 28; accepted 2025 May 8; published 2025 May 22

### **Abstract**

Observations from the Solar Orbiter spacecraft provide unique insights into the interaction between electron beams and the plasma background in the source regions of type III radio emissions. We analyze this interaction by examining the high-frequency electric and magnetic components of in situ wave measurements, focusing on their polarization properties. Using electron data from onboard instruments, we model the electron velocity distribution function and numerically solve the dispersion relation. We compare the predicted polarization of the electric and magnetic components with the observations. Our findings are consistent with propagation in the Langmuir/Z-mode at an oblique wavevector. We explain the magnetic component and transverse polarization by the presence of small density fluctuations, without the need for mode conversion.

*Unified Astronomy Thesaurus concepts:* Solar radio emission (1522); Solar wind (1534); Space plasmas (1544); Plasma physics (2089)

#### 1. Introduction

Type III radio emissions originate from dynamic solar phenomena that release electron beams into the solar wind. These electron beams locally create a positive gradient in the electron velocity distribution function (VDF), leading to the growth of Langmuir waves through kinetic instability (D. Verscharen et al. 2022). These Langmuir waves are key to the subsequent generation of radio emission, although the exact mechanisms of this mode conversion are still under investigation (P. A. Robinson et al. 1994; D. M. Malaspina et al. 2012; V. Krasnoselskikh et al. 2019; I. C. Jebaraj et al. 2023; F. J. Polanco-Rodríguez et al. 2025).

The mechanisms of beam propagation and its interaction with the solar wind remain an area of active research, using both numerical simulations (E. P. Kontar & H. A. S. Reid 2009; C. Y. Lorfing & H. A. S. Reid 2023) and analysis of observational data (C. Y. Lorfing et al. 2023). Previous findings show that instability-driven relaxation of electron beams leads to the formation of a plateau in the VDF. Using STEREO data, D. M. Malaspina & R. E. Ergun (2008) demonstrated that a majority of the Langmuir waves observed in the solar wind exhibit a 1D structure with electric field oscillations aligned with the magnetic field. However, a minority population of waves with transverse polarization has been observed in the Earth's foreshock region (S. D. Bale et al. 1998) and in the solar wind (D. M. Malaspina & R. E. Ergun 2008; D. M. Malaspina et al. 2011), showing a positive correlation between the electron beam velocity and the wave perpendicular energy. To explain the transverse wave polarization, the Z-mode (also referred to as the slow extraordinary mode) branch was proposed, consistent

Original content from this work may be used under the terms of the Creative Commons Attribution 4.0 licence. Any further distribution of this work must maintain attribution to the author(s) and the title of the work, journal citation and DOI.

with the observational data. This was first predicted by theoretical work by D. Krauss-Varban (1989), who also suggested a role of density gradients in the generation of transversely polarized waves. Further research by A. Layden et al. (2011) showed that in a warm magnetized plasma, the characteristics of generalized Langmuir/Z-mode waves change as the waves propagate into regions of differing density. D. B. Graham & I. H. Cairns (2013) then applied the approach of A. Layden et al. (2011) to waves observed by STEREO during type III radio emissions, suggesting electrostatic decay of Langmuir waves.

Waves with a transverse polarization are commonly observed in the solar wind, and it follows that unlike the Langmuir mode they must have a magnetic component. The first observations of the magnetic component during type III bursts were made by the OGO-5 spacecraft, which showed density variations accompanying an enhancement of the spectral density in the magnetic channel (F. L. Scarf et al. 1970). More recently, advanced observations by the Parker Solar Probe provided the first unambiguous observation of the magnetic component of Z-mode waves (A. Larosa et al. 2022).

This study aims to advance the understanding of the waves generated locally by the electron beam and their polarization. Polarization analysis, as suggested by F. L. Scarf et al. (1970), is a critical tool for identification of the wave modes involved.

We analyze wave and particle observations from the Solar Orbiter spacecraft to provide a deeper understanding of the observed waves, which will support future studies on the conversion into radio emission. Our focus lies on the in situ type III emission observed on 2022 October 22 at a heliocentric distance r=0.5 au. We examine both the electron VDF and wave observations, comparing direct field measurements with the wave polarization prediction obtained using a dispersion relation solver based on the susceptibility tensor from the Waves in Homogeneous Anisotropic Multicomponent Plasma

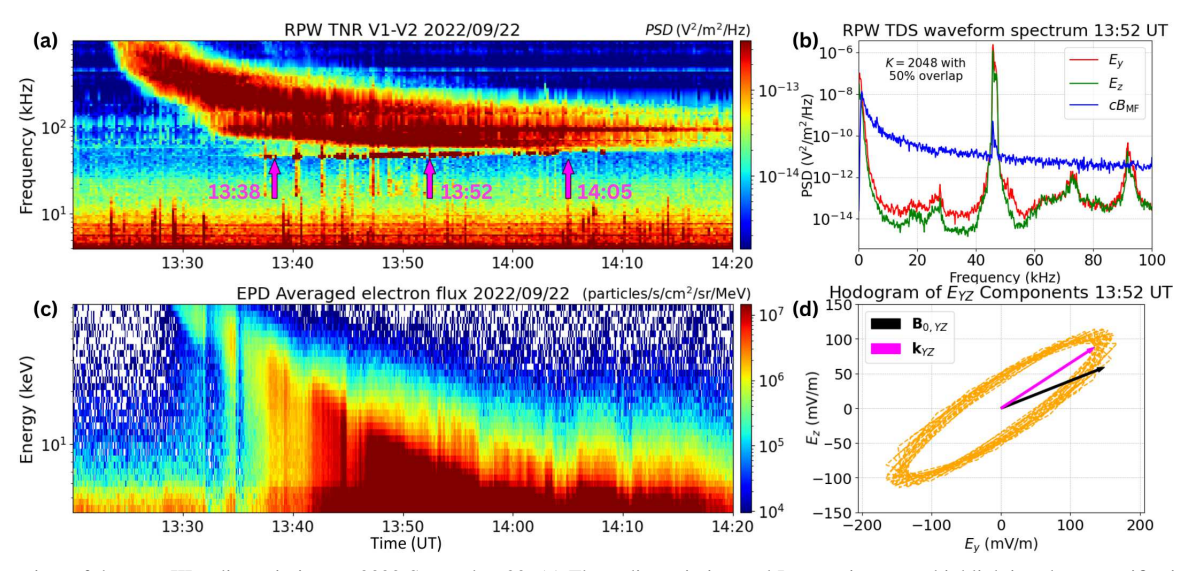


**Figure 1.** Overview of the type III radio emission on 2022 September 22. (a) The radio emission and Langmuir waves, highlighting three specific timestamps. At 13:38 UT and 14:05 UT, we analyze the electron data, while 13:52 UT marks the strongest Langmuir wave observations. (b) Spectrum of the observed waveform at 13:52 UT, including a coherent high-frequency signal from the search coil magnetometer. (c) The averaged electron flux from the STEP instrument. (d) A hodogram of the strongest electric field observations (100 samples), with arrows marking the projection of the ambient magnetic field (black) and the predicted wavevector directions (magenta; more details in Section 4).

(WHAMP) code (K. Roennmark 1982). This work presents the first polarization analysis of the magnetic component of Langmuir/Z-mode waves in the solar wind, identifying the observed wave mode.

The remainder of this Letter is organized as follows: in Section 2, we analyze the observed electron VDF, followed by the numerical solution of the dispersion relation presented in Section 3. Section 4 compares the wave observations with the predictions from the theoretical dispersion relation, and Section 5 concludes the discussion.

## 2. In Situ Observations

For the description of electron VDFs in the solar wind, multiple populations of electrons are typically introduced: the core, halo, strahl, and, in our case, another electron beam population at the keV range of energies (Š. Štverák et al. 2009). To observe these populations, we used the Solar Wind Analyser (SWA; C. J. Owen et al. 2020) and Energetic Particle Detector (EPD; J. Rodríguez-Pacheco et al. 2020) instruments on board the Solar Orbiter.

The SWA Electron Analyser System (EAS) covers energies from 1 eV to 5 keV, capturing the core, halo, and strahl populations with a  $4\pi$  sr field of view. To limit the influence of photoelectrons on the data, we limit our analysis to electron energies above 15 eV. For the energetic electron beam observations, we rely on the SupraThermal Electrons and Protons (STEP) subsystem of EPD, which detects electrons traveling along the nominal Parker spiral direction at energies between 7 and 80 keV. However, the  $28^{\circ} \times 54^{\circ}$  field of view of EPD-STEP limits the availability of electron beam observations to periods when the ambient magnetic field is well aligned with the field of view.

In this study, we focus on the event of 2022 September 22, depicted in Figure 1. We specifically analyze the electron VDF at 13:38 UT and 14:05 UT, as well as the wave observations in between at 13:52 UT. To numerically solve the dispersion relation, we first establish a well-defined model of the electron VDF. This model allows us to use a dispersion solver based on

the susceptibility tensor from the WHAMP code. Since WHAMP requires Maxwellian distributions as input, we represent the VDF as a superposition of multiple Maxwellian distributions, each with its own density, parallel bulk speed, temperature, and anisotropy. This approach enables us to accurately capture the key features of the core, halo, strahl, and beam populations while maintaining compatibility with WHAMP. Specifically, the core and beam populations are each described by a single Maxwellian distribution, while the halo and strahl require multiple Maxwellians to be accurately represented within our framework. While modeling the halo and strahl populations using an anisotropic Kappa distribution offers a viable alternative with fewer parameters (as demonstrated by T. Formánek 2024), we choose not to use this approach to maintain compatibility with WHAMP.

To fit the observed electron VDF, we apply the methodology developed by O. Santolík (1995) and recently examined by G. Nicolaou et al. (2024), which maximizes the Poisson probability of observing  $N_i$  counts for each data point i. The total probability is then

$$P = \prod_{i} p(N_i), \tag{1}$$

where the probability  $p(N_i)$  is given by the Poisson distribution

$$p(N_i) = \frac{e^{-n_i} n_i^{N_i}}{N_i!},$$
 (2)

where  $n_i$  is the model prediction for each data point.

This fitting method enables us to determine the parameters of our model, while the number of Maxwellians is a modeling choice. For the observation at 13:38 UT, we found that using eight Maxwellians was the lowest number that enabled the fit to converge effectively. This choice ensures that the electron beam is represented as a distinct population, while the halo and strahl components consist of distributions with lower bulk velocities compared to the beam velocity. We subsequently used this number of Maxwellians for the other timestamp (14:05 UT). The results of our fits are shown in Figure 2. We

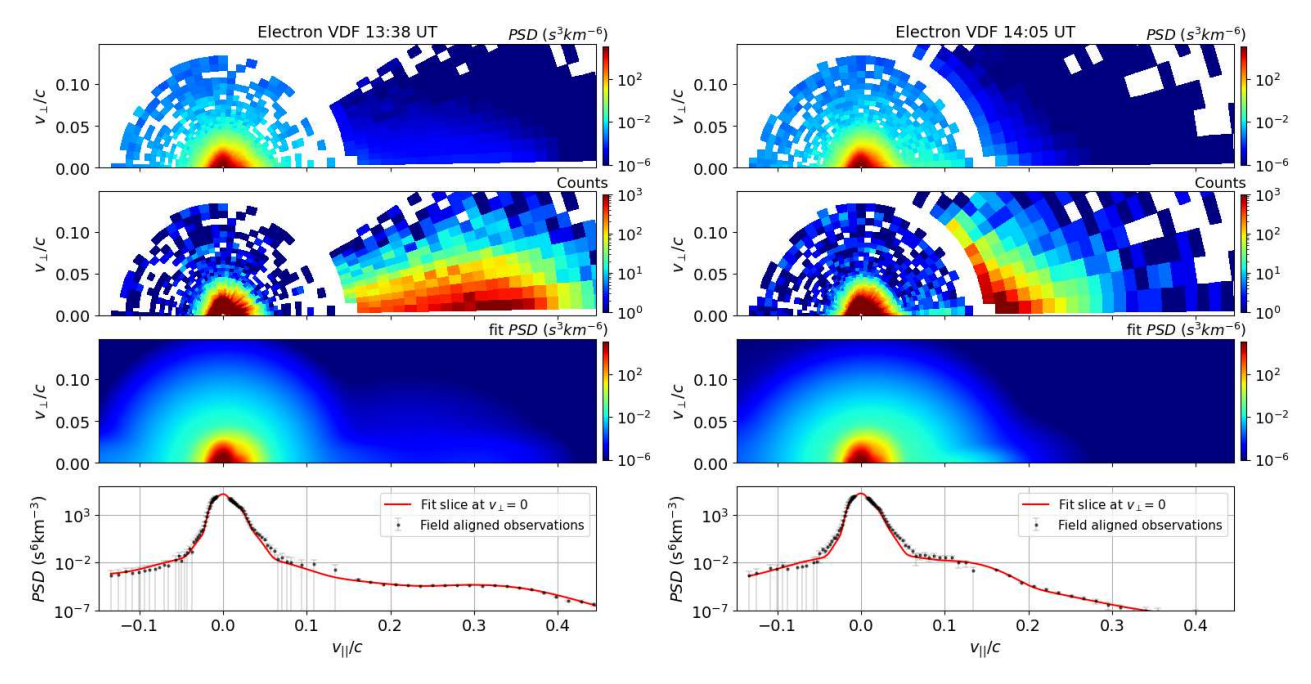


**Figure 2.** In situ electron VDF observations and our model during the type III radio emission on 2022 September 22 are presented. The left column shows observations at 13:38 UT, while the right column shows observations at 14:05 UT. The top two rows combine observations from SWA-EAS and EPD-STEP, displaying phase space density and raw counts. The third row presents the fitted model, and the bottom row shows a slice along the ambient *B* field through the model VDF with observed data points.

observe a distinct beam population at 13:38 UT and a relaxed plateau population at 14:05 UT. Both fitted distributions are marginally stable, which we verified by solving the dispersion relation and by integrating along the perpendicular velocities. This integration yields a single-peaked reduced VDF (not shown here), without a positive gradient at the beam velocity, meeting Gardner's stability theorem (C. S. Gardner 1963).

We use the fitting method described above, and Langmuir wave peak tracking, to accurately determine the parameters of the VDF model. Focusing on two timestamps, 13:38 UT and 14:05 UT, we observe similar key parameters and the evolution of the beam population. At 13:38 UT, the peak tracking provides a number density value of  $n = 25.0 \text{ cm}^{-3}$ and the VDF fitting reveals that 95.5% of the number density corresponds to the thermal core population, with a temperature of 11.7 eV and anisotropy  $A = T_{\perp}/T_{\parallel} - 1$  (C. F. Kennel & H. E. Petschek 1966) of A = 0.70. Similarly, at 14:05 UT, we observe a number density of  $n = 34.7 \text{ cm}^{-3}$ , with the thermal core representing 95.5% of the number density, with a temperature of 11.9 eV and an anisotropy of A = 0.62. These parameters match well with the expected typical solar wind parameters at r = 0.5 au (B. T. Tsurutani et al. 2023). At 13:38 UT, we also identify a distinct electron beam population, representing a fraction  $6.5 \times 10^{-9}$  of the total number density. This electron beam has a temperature of 884 eV, an anisotropy of A = -0.86, and a drift velocity of 23.9 keV. By 14:05 UT, the electron beam with a lower drift velocity has dissipated into a plateau distribution.

The wave observations at the intermediate timestamp of 13:52 UT exhibit the strongest field measurements of the event. These waveform observations are crucial for our polarization analysis since the observed wave shows a transverse polarization and a coherent high-frequency magnetic component. However, the electron VDF observed at that time did not yield a satisfactory fit due to the limitations of our

model, which assumes Maxwellian distributions, and low count statistics. The challenge lies in simultaneously capturing both the beam and plateau populations. Furthermore, at higher energy bins of the EAS, the flux decreases significantly, eventually dropping below the detection threshold in the keV range. At 13:52 UT a significant part of the beam and plateau populations lies in the EAS keV energy range, where the signal is too weak. Consequently, this prevented us from developing a reliable model for the intermediate timestamp. Another consequence of the low count statistics is the need for time averaging, which smooths any rapidly evolving features. To obtain the presented results, we averaged the EPD-STEP data for 60 s and the SWA-EAS data for 600 s. The different durations (centered on the indicated time) have been chosen to provide the same number of records for each bin, since the instruments have a cadence of 1 s for STEP and 10 s for EAS. In triggered mode, the SWA-EAS has a higher cadence by a factor of 10, which would potentially lower the needed averaging time when high cadence data are available for future events.

# 3. Dispersion Relation Solution

To solve the dispersion relation, we use the WHAMP code (K. Roennmark 1982), applying the methodology developed by O. Santolík et al. (2010) and S. Grimald & O. Santolík (2010). In this approach, the susceptibility tensor routine from WHAMP is used along with custom code that handles root finding and normalization. Solving the dispersion relation corresponds to a matrix equation

$$\mathcal{D} \cdot \mathbf{E} = 0, \tag{3}$$

where  $\mathcal{D}$  is the dispersion tensor that depends on both the wavevector  $\mathbf{k}$  and the frequency  $\omega$ . For a given  $\mathbf{k}$  the solver finds the wave frequency  $\omega$  that makes the matrix  $\mathcal{D}$  singular,

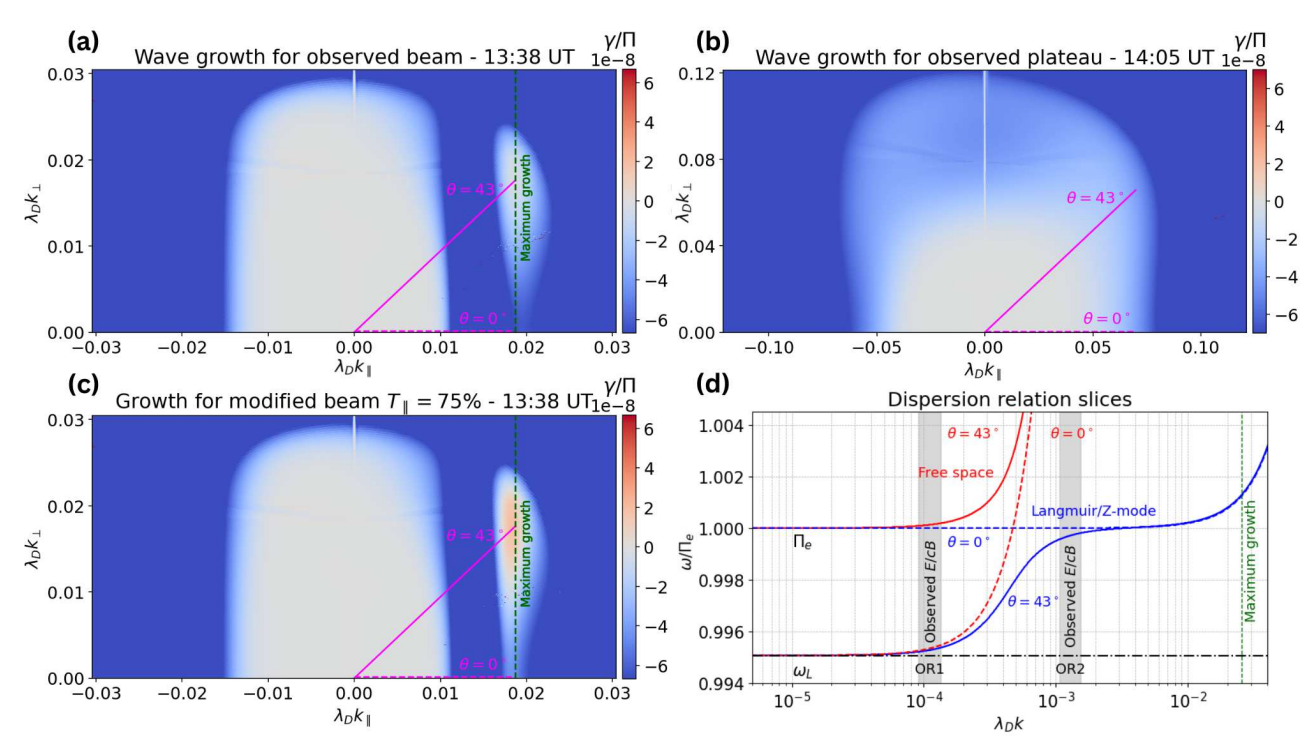


Figure 3. Solutions of the dispersion relation. The wave frequency  $\omega$  and growth rate  $\gamma$  are normalized by the electron plasma frequency  $\Pi_e$ . Panels (a) and (b) show the growth rate obtained for the unmodified distribution at 13:38 UT and 14:05 UT, respectively. (c) The growth rate after reducing the electron beam parallel temperature to 75% at 13:38 UT. The angled line at  $\theta=43^\circ$  between k and k0 corresponds to the maximum growth rate in panels (a) and (c). (d) A slice of the dispersion relation for the generalized Langmuir/Z mode and the free space L-O mode, highlighting in gray two observed regions (ORs) where the observed amplitude ratio E/cB matches with WHAMP.

and we obtain the dispersion relation  $\omega(k)$  and the corresponding complex eigenvectors E. This eigenvector contains the wave polarization information of the electric field components of the wave. Using Maxwell's equations, we can also derive the magnetic field eigenfunction as

$$\mathbf{B} = \frac{\mathbf{k}}{\omega} \times \mathbf{E}.\tag{4}$$

This method provides us with a tool to predict the wave polarization. We can project the computed eigenvectors onto the direction of the antennas, enabling us to study the phase and amplitude differences between any wave components.

Figure 3 presents computed solutions of the dispersion relation. Panels (a) and (b) illustrate the growth rate  $\gamma$  of the observed electron distributions for the 13:38 UT and 14:05 UT timestamps, respectively. These configurations appear marginally stable. To support the presented weak growth rates, we ensured that they are not artifacts of the numerical method. In particular, the WHAMP code uses the Padé approximant, which could introduce systematic errors. To test this approach, we modified the electron beam and plateau populations in our VDF model. The resulting trend of stronger growth rates for more unstable VDFs supports the conclusion that the weak growth rate does not invalidate our results. Furthermore, to address random numerical inaccuracies, the solution was calculated with high resolution in k-space and using double precision in the dispersion solver. To investigate the observed kinetic instability, we modify the VDF at 13:38 UT by lowering the parallel temperature of the electron beam to 75%. This adjustment serves as a simple attempt to reverse the evolution of the VDF caused by wave-particle interactions. However, we cannot directly observe such unstable

distributions because the interactions occur too rapidly to be captured by the electron instruments on board. The result of this modification is shown in Figure 3(c), demonstrating wave growth at oblique wavevectors (not strictly parallel to the magnetic field). Although this modification does not affect the overall electron density or velocity, it slightly increases the growth rate of Langmuir/Z-mode waves above zero. This increase is achieved in a small region of oblique wavevectors. The original unstable VDF is unknown and cannot be reconstructed from available measurements. However, the simple modification of the observed VDF and the corresponding solution in Figure 3(c) demonstrate that wave growth is possible at oblique wavevectors for which the measured VDF implies a marginally stable region in wavevector space (Figure 3(a)). For our observations at 13:38 UT, the lowest damping in this region occurs at an angle  $\theta = 43^{\circ}$  between kand  $B_0$ .

The studied instability is driven by Landau resonance between the electron beam and the  $k_{\parallel}$  component of the wavevector. While this process typically favors waves with parallel propagation, in our case, the maximum growth can be found at oblique angles. This result is explained by the presence of a plateau population in the VDF. In our model, this population is represented by a Maxwellian with a bulk velocity between that of the beam and the core, and with an anisotropy of A=-0.66. We verified the effect of the plateau by calculating the dispersion relation after removing this population, which shifted the maximum growth to parallel wavevectors. One possible interpretation is that, after the plateau population fills the phase space at mainly parallel velocities, resonance shifts to oblique wavevectors, enabling continued scattering into the plateau.

Figure 3(d) presents the dispersion relation of the generalized Langmuir/Z-mode to study the case of  $\theta=43^\circ$ . Comparing this mode with the field-aligned wave and the left-hand polarized free space mode (L-O), we see that the field-aligned free space mode (L) and the generalized Langmuir/Z-mode at  $\theta=43^\circ$  share a similar dispersion relation at  $\lambda_D k \leq 10^{-4}$ .

# 4. Observed Wave Polarization

The presented polarization analysis is based on the assumption that measurements of the phases between the electric and magnetic channels are well calibrated. Besides basic data validation, any direct verification of this assumption using other observations is challenging: the magnetic field is typically below the detection threshold, as in the case of auroral kilometric radiation during the Earth flyby, or the signal coherence is too low due to scattering, as for the radio signal during type III bursts. However, the agreement between observation and theory throughout our analysis is consistent with this assumption, as demonstrated in the following discussion.

To obtain a prediction of the wave polarization from WHAMP, we analyze the dispersion relation and the eigenvectors of the solution. Projecting the eigenvectors onto antenna directions in field-aligned coordinates yields a complex number which describes the component's amplitude and phase. Similarly, for observational data, the recorded waveform observations can be described for a given frequency by the corresponding Fourier coefficient—also containing the amplitude and phase. Using either the WHAMP prediction or waveform observations, we determine the relative phases between components by constructing an averaged spectral matrix

$$S = \begin{bmatrix} \langle E_Y E_Y^* \rangle & \langle E_Y E_Z^* \rangle & \langle E_Y B_{MF}^* \rangle \\ \langle E_Z E_Y^* \rangle & \langle E_Z E_Z^* \rangle & \langle E_Z B_{MF}^* \rangle \\ \langle B_{MF} E_Y^* \rangle & \langle B_{MF} E_Z^* \rangle & \langle B_{MF} B_{MF}^* \rangle \end{bmatrix}.$$
 (5)

The components of S contain information about the wave polarization: taking the argument  $\arg(S_{12})$  provides the relative phase  $\Delta\phi_{EZ}$  between  $E_Y$  and  $E_Z$ , and the diagonal terms are proportional to the power spectral density. Constructing the matrix S for the observed wave  $S_{\rm obs}$  and the WHAMP solution  $S_{\rm WHAMP}$ , we evaluate whether the predicted polarization aligns with the observed data.

Since this dispersion relation solver assumes a gyrotropic VDF, it yields a dispersion relation  $\omega(\mathbf{k})$  that remains invariant under rotations around the direction of the ambient magnetic field. However, the eigenvectors still depend on the choice of the  $\mathbf{k}$  vector. To obtain the correct solution, we need to determine the azimuthal angle  $\alpha$  of the wavevector. We rotate  $\mathbf{k}$  through all azimuthal angles and project the solution eigenfunctions onto the antenna directions in the field-aligned coordinates. This way, we get a matrix function  $\mathbf{S}_{\text{WHAMP}}(\alpha)$ , which we use to determine the predicted polarization.

For the observed waves, we use the waveform observations by the Time Domain Sampler (TDS) of the Radio and Plasma Waves (RPW) instrument (M. Maksimovic et al. 2020). During the studied event, TDS recorded electric and magnetic waveforms at a sampling frequency of 262 kHz. Specifically, the electric field is measured in the Y–Z plane of the Spacecraft Reference Frame (SRF) and the magnetic field component  $B_{\rm MF}$  is recorded by the Search Coil Magnetometer (SCM; G. Jannet et al. 2021) along one axis oriented to (0.5, 0.74, -0.44) in SRF

coordinates. We compute the Fourier components of 2048 sample segments with 50% overlap using a Hann window. We determine the coherences  $C_{ij} = |\langle S_{ij} \rangle| / \sqrt{\langle S_{ii} \rangle \langle S_{jj} \rangle}$  for each frequency and set a threshold of  $C_{YZ}C_{YB}C_{ZB} > 0.7$ . Averaging the result over coherent frequencies (see Figure 4(c)) and the segments within the waveform gives us  $S_{\rm obs}$ , allowing us to determine the observed relative phases as  $\Delta\phi_{YZ} = (-12 \pm 5)^\circ$ ,  $\Delta\phi_{YB} = (-91 \pm 5)^\circ$ , and  $\Delta\phi_{ZB} = (-80 \pm 5)^\circ$ . By averaging the spectral matrix over the snapshot, segments with higher amplitude contribute more, meaning that our results primarily correspond to the polarization during the largest waveform amplitudes.

Now we compare the observed wave polarization with the prediction given by the dispersion relation eigenvectors. In Figure 4 we present the result of our polarization analysis, showing the WHAMP predictions in the first row and the wave observations in the second row. For  $\theta = 43^{\circ}$ , we find that an azimuthal angle of  $\alpha=-30^\circ$  and a wavevector size  $k\lambda_D=1.5\times 10^{-3}$  match with the observations. Our solution of the dispersion relation showed that the maximum growth rate (as seen in Figure 3) occurred at  $k\lambda_D \approx 2.6 \times 10^{-2}$ , suggesting that the wavevector of the observed wave has decreased since its generation, reaching the grayed-out observed region 2 (OR2) in Figures 3(d) and 4(a). In contrast, for wavevectors within OR1, while the theoretical amplitude ratios also match the observations, the relative phases do not agree (not shown). For  $\theta \in (10^{\circ}, 45^{\circ})$ , we also found matching polarization at low wavenumbers around  $10^{-3}\lambda_D^{-1}$ , while outside this range no match was observed.

The wavenumbers matching the observed polarization are 1 order of magnitude lower than the unstable wavenumbers from the linear theory. This can be explained by several mechanisms. Electrostatic decay, as proposed by D. B. Graham & I. H. Cairns (2013), is one possibility. In this process, a primary Langmuir wave decays into a secondary Langmuir/Z-mode wave with a lower wavenumber and a low-frequency ion-acoustic wave. While our observations do not rule out this mechanism, the absence of a clear double peak in the frequency spectrum might favor other explanations.

Another possible mechanism, studied by D. M. Malaspina et al. (2011), is that the wavenumber decreased due to propagation into density gradients. As demonstrated by Figure 3(d), the required change in the plasma frequency would be very small, close to 0.1%. Additionally, even if stronger instabilities tend to favor parallel wave growth, a density gradient misaligned with  $B_0$  could refract the wave. In this case, an initially parallel Langmuir wave could be transformed into an oblique Langmuir/Z-mode wave. Although we were able to constrain the wavevector to the OR2 region, where the relative phases and amplitudes are consistent with the WHAMP solution, we cannot definitively determine which of the proposed mechanisms is responsible for the observed wave properties.

We performed the polarization analysis on waves recorded at 13:52 UT because the waveform data show the strongest electric field observations. In Figure 1(d), we show the hodogram of these observations with the directions of the WHAMP predicted wavevector and the observed ambient magnetic field direction (projected onto the SRF *Y–Z* plane). We see that the observed wave has an elliptical polarization, with the major axis not aligned with the magnetic field but well aligned with the calculated wavevector, just as predicted by

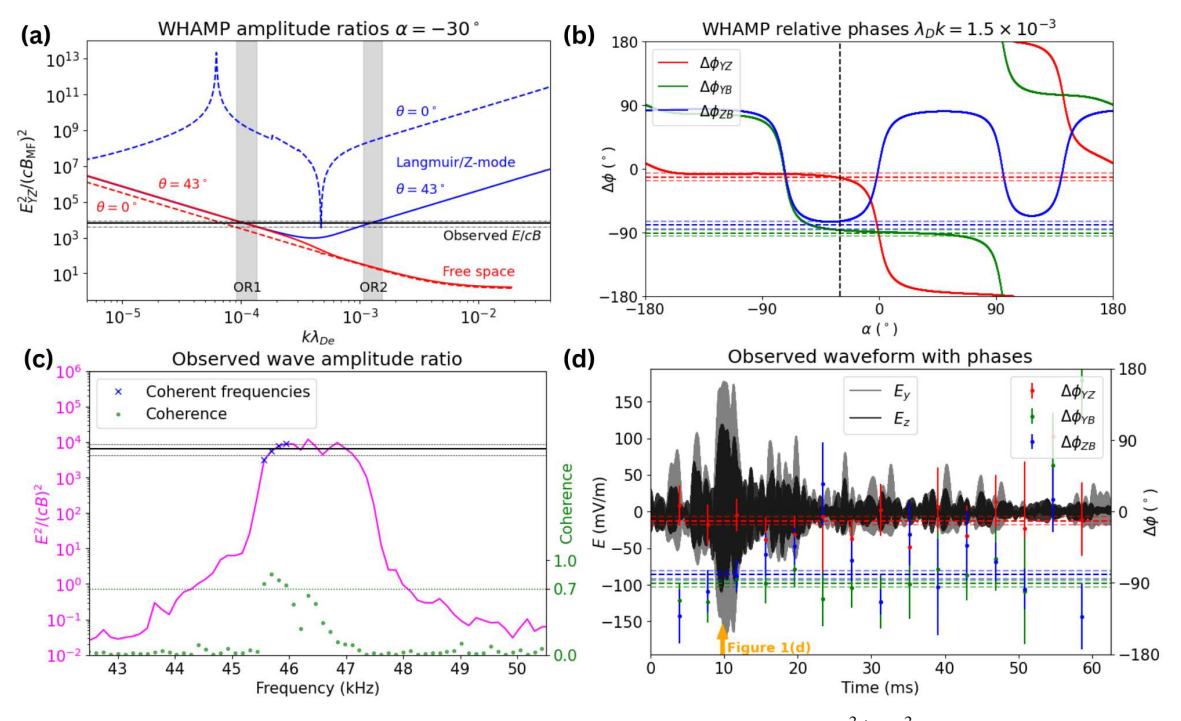


**Figure 4.** Analysis of the observations at 13:38 UT. (a) The WHAMP predictions for the amplitude ratios of  $E^2/(cB)^2$  as a function of the wavevector modulus for (blue lines) the Langmuir/Z mode and (red lines) the free space L-O mode, for (solid lines) wavevectors at 43° from the local magnetic field direction, and for (dashed lines) field-aligned wavevectors. The black lines show the observed E/cB ratio from panel (c) with experimental uncertainties. (b) Predicted relative phases between wave components as a function of the azimuthal angle of the wavevector. Dashed lines show the experimentally determined values from panel (d) with their experimental uncertainties. (c) The observed values of the amplitude ratios along with the wave coherence in frequency space. (d) The observed waveform, highlighting the evolution of phases between components.

WHAMP. In general, the WHAMP solution predicts a linear polarization of the electric field fluctuations when k is aligned with the magnetic field line and an elliptical polarization at higher wavevector angles  $\theta$ .

Suppose that the observed wave has propagated from its generation region into a region of higher density. It has remained at the original frequency of maximum growth (see Figure 3(d)), while the entire dispersion curve (blue line in Figure 3(d)) has shifted upward along the frequency axis, thus decreasing the magnitude of its wavevector. To allow the wave to propagate to a higher density plasma, it must not be strongly damped by the "valley" of negative growth rate observed in Figure 3(c), which lies between the region of beam growth and the small-wavenumber region of weak damping. This can occur in the presence of a plateau, as demonstrated in Figure 3(b), or when the density change happens sufficiently fast over a smaller distance than the wavelength of the wave.

This analyzed wave was recorded between the neighboring timestamps of 13:38 UT and 14:05 UT, during which we found a solution to the dispersion relation. We replicated the same results of the polarization analysis using both timestamps with a similar outcome (not shown). For this reason, we suppose that for the intermediate timestamp we can also use the same results.

## 5. Conclusions

We performed a polarization analysis of the Langmuir/Z-mode waves observed during an in situ type III radio emission. The first of their kind observations of a coherent magnetic component allowed us to compare the electric and magnetic waveform observations from RPW with a prediction. This

analysis was made possible by the availability of in situ electron observations by the SWA and EPD instruments. By modeling the electron VDF and solving the dispersion relation, we showed that the observed wave polarization is consistent with obliquely propagating generalized Langmuir/Z-mode waves. The observed relative amplitudes and phases of fluctuating electric and magnetic fields correspond to wavenumbers around  $10^{-3}\lambda_D^{-1}$ . Linear solution of the dispersion relation reveals that these waves can grow at oblique wavevectors but with significantly larger wavenumbers compared to the observations. Propagation into density gradients can be responsible for this wavenumber shift. Growth at parallel wavevectors and subsequent refraction at density gradients can also possibly explain the observations. Our findings are consistent with the concepts proposed by D. Krauss-Varban (1989) and A. Layden et al. (2011), and with the wavenumber shifting mechanisms considered by D. M. Malaspina et al. (2011).

## Acknowledgments

This work was supported by state funding under the France 2030 program, managed by the French National Research Agency (ANR), reference ANR-23-CMAS-0041. The authors acknowledge the financial support provided by the GAČR grant 22-10775S. M.K. acknowledges funding from the CNES for the Solar Orbiter/RPW instrument. Solar Orbiter is a mission of international cooperation between ESA and NASA, operated by ESA. Solar Orbiter SWA data were derived from scientific sensors that were designed and created and are operated under funding provided by numerous contracts from UKSA, STFC, the Italian Space Agency, CNES, the French

National Centre for Scientific Research, the Czech contribution to the ESA PRODEX program, and NASA. Solar Orbiter SWA work at the UCL/Mullard Space Science Laboratory was funded by STFC (grant Nos. ST/W001004/1 and ST/X/002152/1).

## **ORCID iDs**

```
Tomáš Formánek https://orcid.org/0000-0003-4766-638X Ondřej Santolík https://orcid.org/0000-0002-4891-9273 Jan Souček https://orcid.org/0000-0003-0462-6804 David Píša https://orcid.org/0000-0002-1322-7576 Arnaud Zaslavsky https://orcid.org/0000-0001-8543-9431 Matthieu Kretzschmar https://orcid.org/0000-0001-5796-6138 Milan Maksimovic https://orcid.org/0000-0001-6172-5062 Christopher J. Owen https://orcid.org/0000-0002-5982-4667 Georgios Nicolaou https://orcid.org/0000-0003-3623-4928
```

#### References

```
Bale, S. D., Kellogg, P. J., Goetz, K., & Monson, S. J. 1998, GeoRL, 25, 9
Formánek, T. 2024, Bachelor thesis, Charles Univ., Praha, http://hdl.handle.net/20.500.11956/191324
Gardner, C. S. 1963, PhFl, 6, 1366
Graham, D. B., & Cairns, I. H. 2013, JGRA, 118, 3968
Grimald, S., & Santolík, O. 2010, JGRA, 115, 2009JA014997
Jannet, G., Dudok De Wit, T., Krasnoselskikh, V., et al. 2021, JGRA, 126, e2020JA028543
```

```
Jebaraj, I. C., Krasnoselskikh, V., Pulupa, M., Magdalenic, J., & Bale, S. D.
  2023, ApJL, 955, L20
Kennel, C. F., & Petschek, H. E. 1966, JGR, 71, 1
Kontar, E. P., & Reid, H. A. S. 2009, ApJ, 695, L140
Krasnoselskikh, V., Voshchepynets, A., & Maksimovic, M. 2019, ApJ,
Krauss-Varban, D. 1989, JGRA, 94, 3527
Larosa, A., Dudok De Wit, T., Krasnoselskikh, V., et al. 2022, ApJ, 927, 95
Layden, A., Cairns, I. H., Robinson, P. A., & LaBelle, J. 2011, JGRA, 116,
  A12328
Lorfing, C. Y., & Reid, H. A. S. 2023, SoPh, 298, 52
Lorfing, C. Y., Reid, H. A. S., Gómez-Herrero, R., et al. 2023, ApJ, 959, 128
Maksimovic, M., Bale, S. D., Chust, T., et al. 2020, A&A, 642, A12
Malaspina, D. M., Cairns, I. H., & Ergun, R. E. 2011, GeoRL, 38, L13101
Malaspina, D. M., Cairns, I. H., & Ergun, R. E. 2012, ApJ, 755, 45
Malaspina, D. M., & Ergun, R. E. 2008, JGRA, 113, 2008JA013656
Nicolaou, G., Livadiotis, G., Sarlis, N., & Ioannou, C. 2024, RASTI, 3, 874
Owen, C. J., Bruno, R., Livi, S., et al. 2020, A&A, 642, A16
Polanco-Rodríguez, F. J., Krafft, C., & Savoini, P. 2025, ApJL, 982, L24
Robinson, P. A., Cairns, I. H., & Willes, A. J. 1994, ApJ, 422, 870
Rodríguez-Pacheco, J., Wimmer-Schweingruber, R. F., Mason, G. M., et al.
  2020, A&A, 642, A7
Roennmark, K., 1982 Waves in Homogeneous Anisotropic Multicomponent
  Plasmas (WHAMP), GitHub
Santolík, O. 1995, PhD thesis, Charles Univ., Praha
Santolík, O., Gurnett, D. A., Pickett, J. S., et al. 2010, JGRA, 115,
  2009JA015218
Scarf, F. L., Fredricks, R. W., Green, I. M., & Neugebauer, M. 1970, JGR,
  75, 3735
Štverák, Š., Maksimovic, M., Trávníček, P. M., et al. 2009, JGRA, 114,
  A05104
Tsurutani, B. T., Zank, G. P., Sterken, V. J., et al. 2023, ITPS, 51, 1595
Verscharen, D., Chandran, B. D. G., Boella, E., et al. 2022, FrASS, 9, 951628
```